



# Intercellular mitochondrial transfer contributes to microenvironmental redirection of cancer cell fate

Julie Sofie Bjerring, Yara Khodour, Emilee Anne Peterson, Patrick Christian Sachs  and Robert David Bruno 

School of Medical Diagnostics and Translational Sciences, College of Health Sciences, Old Dominion University, Norfolk, VA, USA

## Keywords

3D bioprinting; breast cancer; cellular redirection; microenvironment; mitochondrial transfer

## Correspondence

R. D. Bruno, Old Dominion University,  
Health Sciences Building, 2 Rm 3051, 1019  
W. 41st Street, Norfolk, VA 23508, USA  
Tel: +1 757 683 7091  
E-mail: [rbruno@odu.edu](mailto:rbruno@odu.edu)

and

P. C. Sachs, Old Dominion University,  
Health Sciences Building, 2 Rm 3042, 1019  
W. 41st Street, Norfolk, VA 23508, USA  
Tel: +1 757 683 7090  
E-mail: [psachs@odu.edu](mailto:psachs@odu.edu)

Patrick Christian Sachs and Robert David  
Bruno contributed equally to this work.

(Received 23 May 2024, revised 4 October  
2024, accepted 30 December 2024)

doi:10.1111/febs.70002

The mammary microenvironment has been shown to suppress tumor progression by redirecting cancer cells to adopt a normal mammary epithelial progenitor fate *in vivo*. However, the mechanism(s) by which this alteration occurs has yet to be defined. Here, we test the hypothesis that mitochondrial transfer from normal mammary epithelial cells to breast cancer cells plays a role in this redirection process. We evaluate mitochondrial transfer in 2D and 3D organoids using our unique 3D bioprinting system to produce chimeric organoids containing normal and cancer cells. We demonstrate that breast cancer tumoroid growth is hindered following interaction with mammary epithelial cells in both 2D and 3D environments. Furthermore, we show mitochondrial transfer occurs between donor mammary epithelial cells and recipient cancer cells primarily through tunneling nanotubes (TNTs) with minimal amounts seen from extracellular transfer of mitochondria, likely via extracellular vesicles (EVs). This organelle exchange results in various cellular and metabolic alterations within cancer cells, reducing their proliferative potential, and making them susceptible to microenvironmental control. Our results demonstrate that mitochondrial transfer contributes to microenvironmental redirection of cancer cells through alteration of metabolic and molecular functions of the recipient cancer cells. To the best of our knowledge, this is the first description of a 3D bioprinter-assisted organoid system for studying mitochondrial transfer. These studies are also the first mechanistic insights into the process of mammary microenvironmental redirection of cancer and provide a framework for new therapeutic strategies to control cancer.

## Introduction

While there is a growing body of evidence about the pro-tumorigenic microenvironment created surrounding cancerous growths [1–3], how the normal microenvironment drives the process of cancer cell suppression is understudied. Our group and colleagues have shown that the normal mammary gland has an extraordinary ability to ‘redirect’ cancerous and nonmammary cells to adopt a normal mammary epithelial cell fate [4–9].

Specifically, these redirection studies used NTERA-2 teratocarcinoma, mouse MMTV-*neu* and HER2<sup>+</sup> cancer cells, neural stem cells, testicular cells, and human breast cancer cells mixed with normal mouse mammary epithelial cells (MECs) and co-injected into epithelial devested fat pads of mice [4,6–10]. The resulting regenerated mammary glands epithelial trees consisted of integrated MECs and redirected nonmammary cells

## Abbreviations

Bcl-2, B-cell lymphoma 2; BFP, blue fluorescent protein; CNC, computer numerical controlled; EVs, extracellular vesicles; GFP, green fluorescent protein; MECs, normal mouse mammary epithelial cells; RFP, red fluorescent protein; ROS, reactive oxygen species; TNT, Tunneling nanotubes.

that displayed normal MEC morphology and function. The redirected cancer cells persisted and self-renewed through pregnancy, lactation, and multiple transplant generations, demonstrating they had not undergone terminal differentiation or senescence but rather had adopted a normal progenitor cell fate. While it is undoubtedly a complex process, if we can fully understand how the normal mammary microenvironment can control and revert cancer cells, we will be able to develop new paradigms that could prevent women from having to go through the trauma of breast cancer altogether. Unfortunately, mechanistic insights into the process are lacking, which prevents these incredible basic science findings from becoming translational approaches in the fight against breast cancer.

To begin dissecting the molecular mechanisms underlying microenvironmental control of cell fate, it is necessary to implement robust and adjustable experimental parameters *in vitro* [11]. Standard culture methods only rarely produce chimeric mammary organoids [12,13]. This is because mixed cell populations in 3D cultures fail to aggregate together efficiently using standard techniques. To circumnavigate this problem, we have developed a novel 3D bioprinter system capable of generating consistent human mammary/cancer cell chimeric organoids that mimic our *in vivo* findings [12,14,15] (Fig. 1; Video S1). A critical feature of this bioprinter is its ability to produce these organoids in a highly repeatable fashion due to its computer numerically controlled (CNC) driven positional accuracy [15]. The open-source printing platform can control single-cell placement within preformed hydrogels down to approximately 10  $\mu\text{m}$  in all three-dimensional planes (X, Y, and Z) [14]. Thus, the accuracy of our printing system allows us to cluster mixed populations within a very small volume (<10 nL) in any coordinate 3D space in any hydrogel. This allows our group to generate consistent large, grided quantities of human breast epithelial structural organoids and chimeric organoids resembling our *in vivo* findings [12,14].

Interestingly, in recent years, research has established a process of mitochondrial transfer between cells [16–22]. Various somatic and stem cell types can exchange mitochondria and other cellular content, providing a critical role in tissue homeostasis, damaged tissue repair, and tumor progression under physiological conditions [17,21]. Importantly, because mitochondrial transfer has been shown to rescue stress-induced cells, this behavior allows insight into the cellular microenvironment and how cell communication between phenotypically normal tissue and metabolically stressed cells can alter fate redirection and lead to cellular rejuvenation. Therefore, we reasoned that

mitochondrial transfer might be a potential component of mammary microenvironmental redirection of breast cancer cells, which would alter their metabolic responses to allow for normal cellular function.

In this paper, we demonstrate for the first time that mitochondrial transfer contributed to the microenvironmental redirection of cancer cell fate using a 3D bioprinted *in vitro* model. We show that in 3D bioprinted organoids, normal mammary epithelium contributes mitochondria to cancer cells. This organelle exchange leads to alterations in metabolic markers and gene expression resulting in sustained reduction in tumoroid growth. These findings are the first potential mechanistic insight into the control of cancer by the normal mammary microenvironment. This is vital as researching the metabolic power and various effects of microenvironmental signaling yields powerful new therapeutic and diagnostic tools for the fight against cancer.

## Results

### Breast cancer tumoroid growth is inhibited following interaction with normal mammary epithelial cells

Previous studies have shown that both human and mouse cancer cells can be redirected to adopt normal mammary progenitor cell fates *in vivo* [6,7,10] and take part in normal luminal organoid formation *in vitro* [23]. However, limited studies have investigated the long-term effects this process has on the cancer cells once they are removed from the normal suppressive microenvironment. To study this, MCF-7 cells were transduced with a CAG promoter-driven RFP containing a puromycin selection gene. MCF-7 cells were cocultured with normal mammary epithelial MCF-12a cells or unlabeled MCF-7 cells as controls. After 48 h of puromycin selection, the unlabeled cells were killed off, and the remaining cancer cells from the 2D cultures were 3D printed in arrays of  $3 \times 10$  into rat tail collagen hydrogels and grown over a 7-day period. After the initial 7 days establishing our 100% tumor size, tumoroids were then also measured for an additional 7-day period. It was seen that growth patterns were greatly decreased when the cancer cells were extracted from 2D cocultures with MCF-12a epithelial cells compared to MCF-7 control prints (Fig. 2A). Next, we repeated the experiment in 3D by bioprinting arrays of chimeric mammary organoids containing MCF-12a and MCF-7 RFP cells and then killed off the MCF-12a with puromycin (Fig. 2B). Hybrid tumoroids containing MCF-7 RFP and unlabeled MCF-7 cells were used as controls. After removal of the MCF-12a cells, MCF-7 RFP cells formed tumoroids at a significantly

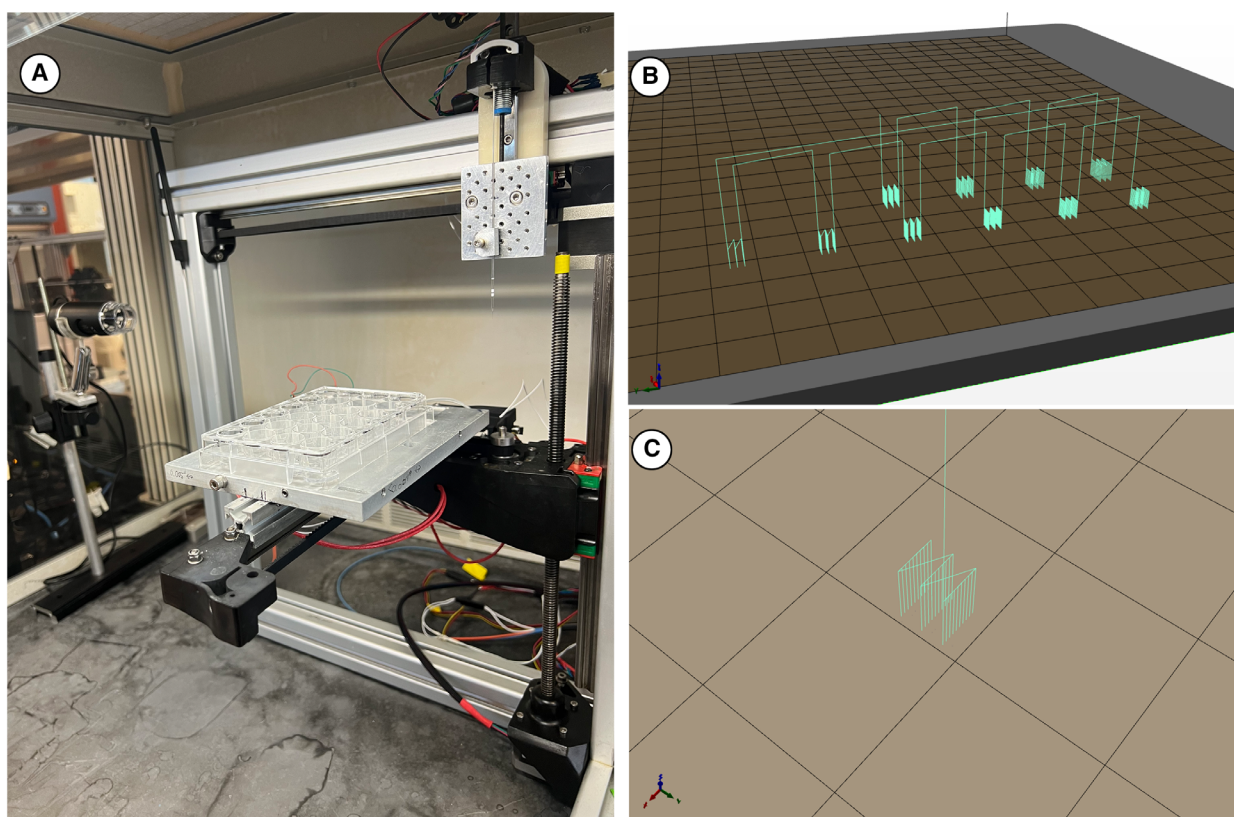


**Fig. 1.** 3D bioprinter. (A) Image of laboratory low-cost 3D bioprinter setup. (B, C) Visual representation of instructional GCODE for printing procedure of 10 wells (B) and a singular well (C) in 3D hydrogels.

reduced rate when compared to controls (Fig. 2B). To eliminate the effects of puromycin, we used FACS to separate the RFP-labeled MCF-7 cells from the noncancerous cell population when cocultured in 2D. Similarly, the purified MCF-7s grew significantly slower than control MCF-7 cells (Fig. 2C). Notably, in all cases, the morphology of the MCF-7 growths was condensed tumoroids and no evidence of luminal formation was seen when removed from the MCF-12a microenvironment. This was consistent with previous reports that showed that MMTV-*neu* cancer cells reverted to a tumorigenic fate when removed from chimeric mammary glands *in vivo* but had a reduced tumor growth rate [10]. Together, these results demonstrate that while redirection is reversible, the process does have sustained effects on cancer cell growth, suggesting persistent changes occur within the cancer cells.

To further evaluate the effects of the mammary epithelial microenvironment on cellular reprogramming of breast cancer cells, Ki67, a common proliferative marker and tool for cancer diagnostics, was examined in both control and cocultured MCF-7 cell populations. Using antibody immunofluorescent staining,

Ki67 protein levels were quantified in 2D cultures. The proliferative marker was determined to be approximately 2.5 times as prevalent in the MCF-7 control population when compared to the cancerous cells from the cocultured environment ( $****P < 0.0001$ ) (Fig. 3A–C). This emphasizes that microenvironmental signals cause fate redirection of MCF-7 cells, which leads to a significant decrease in proliferation and tumoroid growth. Additionally, the prevalence of apoptosis was evaluated using an annexin V conjugate GFP kit. More in line with normal cell behavior, it was found that MCF-7 from the cocultured environment had significantly lower amounts of apoptotic cells than MCF-7 cells isolated from control plates ( $*P = 0.0429$ ,  $*P = 0.0353$ ) (Fig. 3D–F).

### Normal mammary epithelial cell lines transfer mitochondria to breast cancer cells within chimeric structures

We hypothesized that mitochondrial transfer plays a role in metabolic signaling for chimeric structures and aids in breast cancer cell fate redirection. To test this,



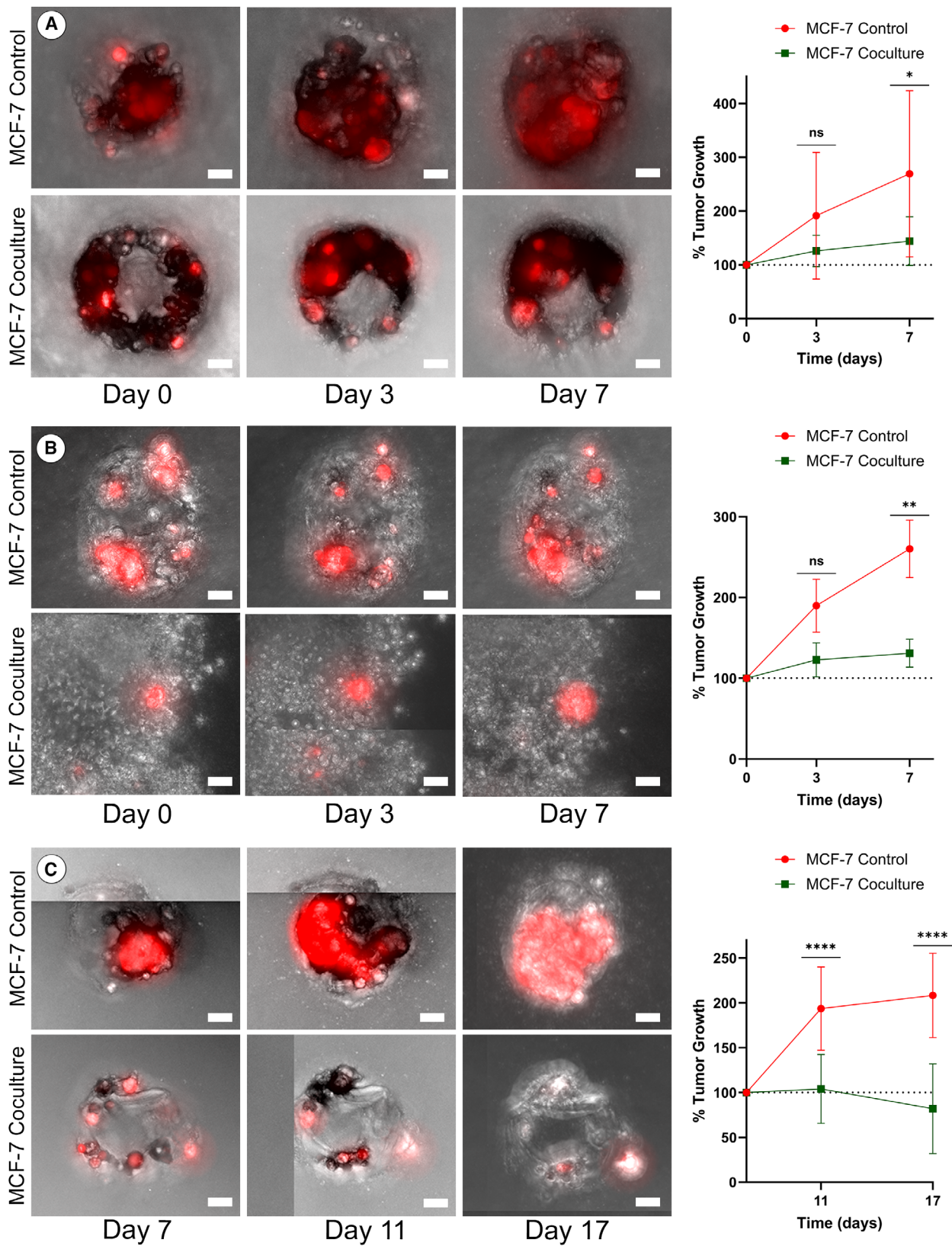




**Fig. 2.** Tumoroid growth of MCF-7 mammary cancer cells following interaction with MCF-12a cells. (A) MCF-7 RFP cells were cocultured with unlabeled MCF-12a cells or unlabeled MCF-7 cells (controls). The MCF-12a and MCF-7 cells were killed off by 48-h puromycin selection treatment. Surviving MCF-7 RFP cells were bioprinted into rat tail collagen hydrogels. Left: Representative image of 3D printed MCF-7 (red) mammary tumoroids on days 0, 3, and 7 after initial 7-day tumoroid formation. Right: Graph of the mean percentage of tumoroid growth demonstrating significant decrease in growth rate when MCF-7 cells are isolated from MCF-12a cocultures ( $*P < 0.05$ ;  $n = 11$ ). (B) MCF-7 RFP cells were 3D printed with MCF-12a cells or unlabeled MCF-7 cells (control) in rat tail collagen. Organoids/tumoroids formed over a 7-day period followed by an additional 7 days of puromycin treatment. Left: Representative images captured on day 0, 3, and 7 postpuromycin treatment. Right: Graph of the mean percentage of tumoroid formation demonstrating significant decrease in growth rate following 3D coculture with MCF-12a cells ( $**P < 0.01$ ;  $n = 11$ ). (C) MCF-7 RFP cells were cocultured with MCF-12a cells or unlabeled MCF-7 cells (controls) and then isolated by fluorescence-activated cell sorting (FACS) and 3D printed into rat tail collagen hydrogels. Left: Representative images of tumoroids captured on day 7, 11, and 17 postprint. Right: Graph of the mean percentage of tumoroid growth demonstrating significant decrease in tumoroid growth rate when MCF-7 cells are isolated from MCF-12a cocultures ( $****P < 0.0001$ ;  $n = 10$ ). All statistical data were analyzed using a two-way analysis of variance (ANOVA) with a Tukey multiple comparison test. Error bars represent standard deviation (SD). Scale bars = 20  $\mu\text{m}$ .

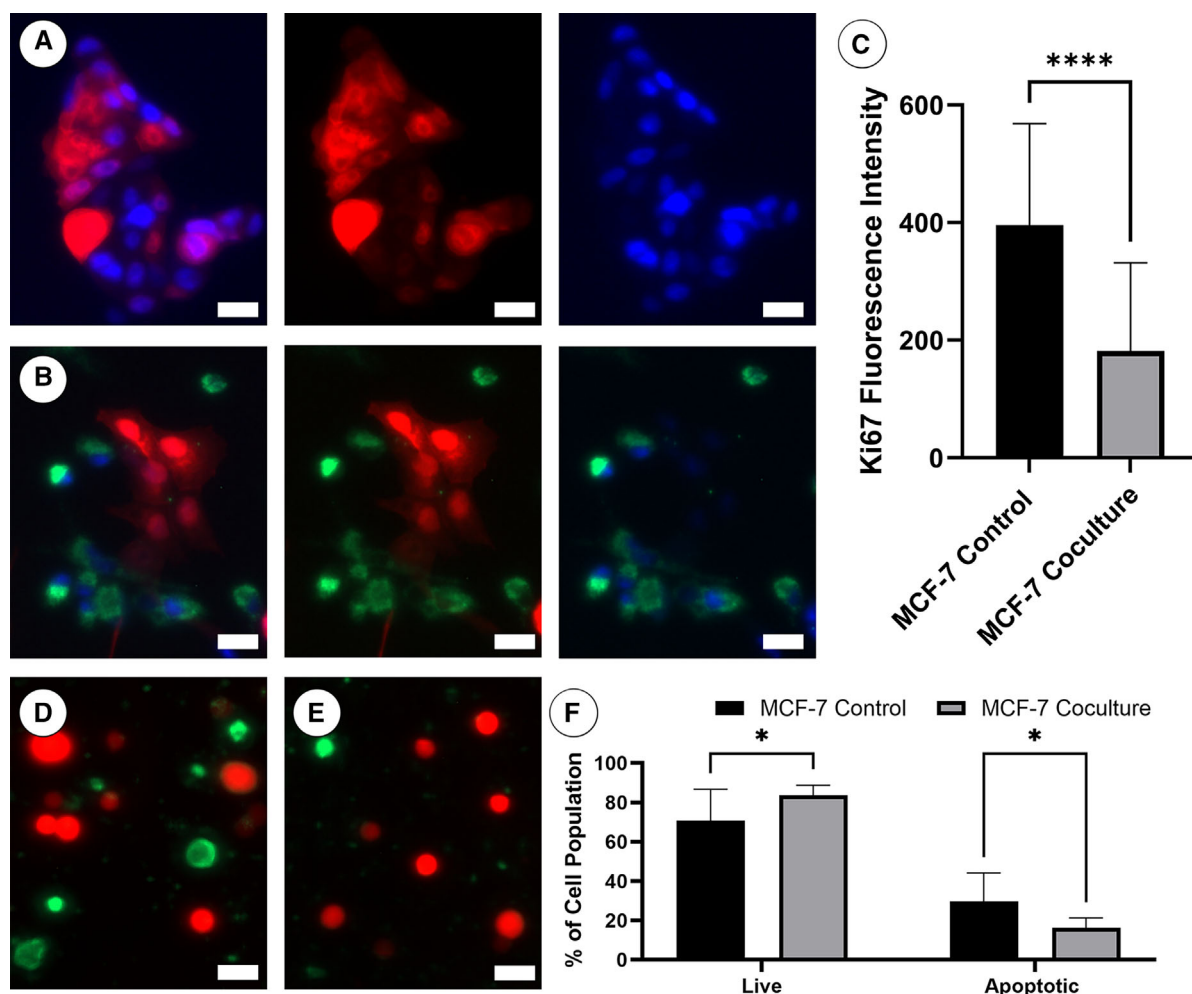


**Fig. 3.** Cell proliferation of MCF-7 mammary cancer cells decreases following interactions with MCF-12a cells. (A, B) Immunofluorescence staining of Ki67 (blue) on control MCF-7 RFP cells (red) (A), and cocultured MCF-12a-Mito-GFP (green) and MCF-7 RFP (red) (B). (C) Quantification of the mean fluorescent intensity of Ki67 comparing MCF-7 control ( $n = 55$ ) and MCF-12a/MCF-7 coculture populations ( $n = 40$ ) ( $****P < 0.0001$ ). (D, E) Annexin V Conjugates for apoptosis analysis displaying green (apoptotic) and red (live) cells from MCF-7/MCF-7 RFP (control) (A) and MCF-12a/MCF-7 RFP cocultures. (F) Quantification of the mean percent of live ( $*P = 0.0429$ ) and apoptotic cells ( $*P = 0.0353$ ) ( $n = 540$ ) in control MCF-7/MCF-7 RFP and MCF-12a/MCF-7 RFP cocultures. Error bars display standard deviation (SD) of the mean. All statistical data were analyzed using an unpaired *t*-test. Scale bars = 20  $\mu\text{m}$ .

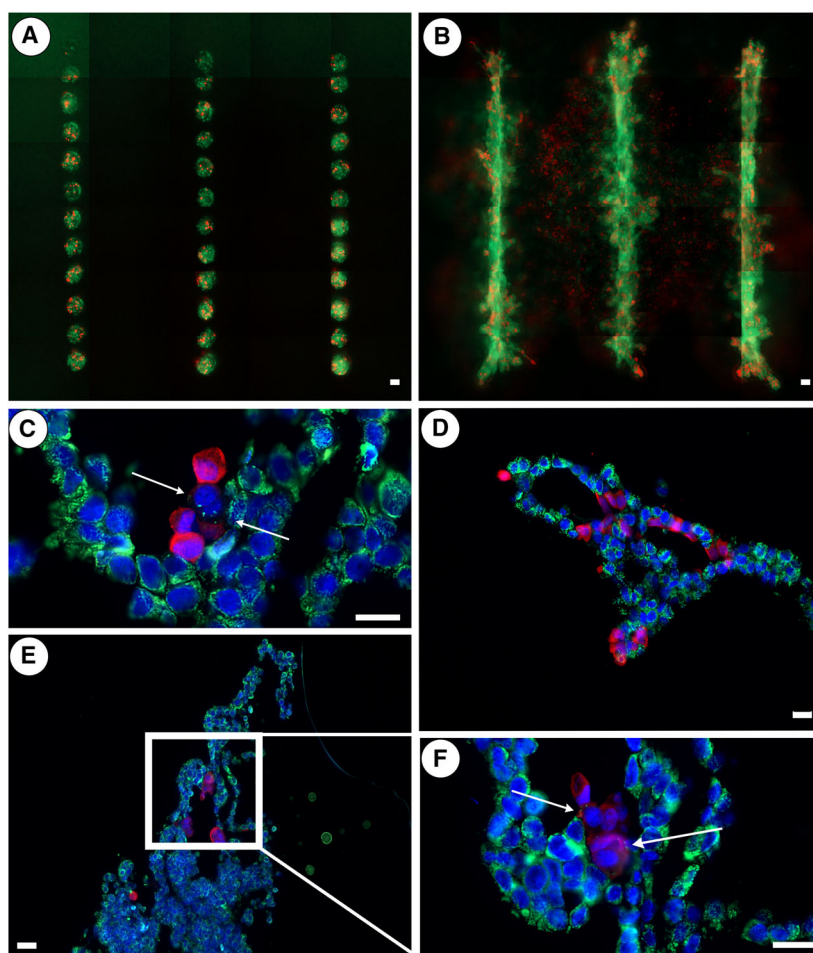


**Fig. 4.** Mitochondrial transfer within 3D bioprinted chimeric organoids. (A, B) Example of 3D printed chimeric organoid in rat tail collagen containing 100 cells per injection in a 5:1 ratio of MCF-12a-Mito-GFP (green) and MCF-7 RFP (red) cells printed in a three column (1.5 mm), 12 row (300  $\mu$ m) formation at day 1 (A), and day 10 (B). (C) Immunofluorescence staining of a 5  $\mu$ m cross-section of bioprinted chimera. White arrows showing MCF-12a-derived mitochondria integrated into MCF-7 RFP cells. Figure representative of 45 cells from 8 slides obtained over 5 independent experiments. (D, E) Immunofluorescence staining of 5  $\mu$ m cross-section of bioprinted chimera showing MCF-12a Mito-GFP-mammary epithelial and MCF-7 RFP cancer cells forming integrated luminal organoids mimicking *in vivo* mammary structures. Figure representative of (D) 98 cells (E) 567 cells from 8 slides obtained over 5 independent experiments. (F) Centralized image of (E) using white arrows to show immunofluorescence staining of 5  $\mu$ m cross-section of bioprinted chimera showing MCF-12a-derived mitochondria integrated into MCF-7 RFP (red) cells. Figure representative of 68 cells from 8 slides obtained over 5 independent experiments. All sections are counterstained with DAPI (blue). All samples were analyzed 10-day postprint. Scale bars: a, b = 100  $\mu$ m; c–f = 20  $\mu$ m.

we used a lentivirus system to permanently label mitochondria in epithelial mammary cells for mitochondria tracking. The lentivirus system labels mitochondria with CopGFP by using a peptide tag to cytochrome C oxidase subunit VIII. Then, using methods previously described by our group [12,23], we implemented our 3D bioprinter to generate chimeric organoids consisting of MCF-12a Mito-GFP and MCF-7 RFP cells (Fig. 4A). As demonstrated previously [23], these cells formed long, linear, luminal organoids over a 10–14 day period (Fig. 4B). Importantly, it was observed that MCF-7 RFP cells were integrated into

the epithelial cell organoids, forming a chimeric cellular network (Fig. 4D). Immunostaining revealed that CopGFP-labeled mitochondria were inside of MCF-7 RFP cells (Fig. 4C,E,F). This shows that mitochondria travel from the donor MCF-12a and successfully transfer into recipient MCF-7 cells in 3D bioprinted organoids. Overall, 14.94% of all MCF-7 found within the 3D microenvironment displayed evidence of mitochondrial transfer from the donor MCF-12a (Table 1). Importantly, the CopGFP tag is nuclear encoded, and thus, the quantitation is limited as it is diluted out once it leaves the MCF-12a cells.

**Table 1.** Frequency of mitochondrial transfer observed through tunneling nanotubes and extracellular vesicles.

Donor MCF12A transfer to recipient:	Total recipient cells w/Mito transfer in 2D	Total recipient cells w/Mito transfer in 3D	Total recipient cells w/Mito transfer after TNT inhibition (Cytochalasin D)	Total recipient cells w/Mito transfer after conditioned medium exposure	Total recipient cells w/Mito transfer after EV inhibition (ROCK inhibitor)	P-value
MCF-7	19.77% ( <i>n</i> = 1143)	14.94% ( <i>n</i> = 117)	3.00% ( <i>n</i> = 406)	2.41% ( <i>n</i> = 978)	0.58% ( <i>n</i> = 1024)	<0.0001***
MDA-MB-231	21.35% ( <i>n</i> = 609)	N/A	N/A	4.67% ( <i>n</i> = 236)	N/A	0.0004***
MMTV- <i>neu</i>	5.88% ( <i>n</i> = 594)	N/A	N/A	5.03% ( <i>n</i> = 191)	N/A	0.7163 ns

\*\*\**P* < 0.001; \*\*\*\**P* < 0.0001.

Comparably, 2D experimentation was completed to determine if similar mitochondrial transfer occurs in alternative human and mouse cancer cell 2D cultures. MCF-12a Mito-GFP cells were cultured with MCF-7 RFP or MDA-MB-231 RFP cancer cells at a 2:1 ratio, respectively, over a 48-h period. The timeframe was selected as it was determined that mitochondrial transfer occurs as early as 24 h postpassage. The rate of mitochondrial transfer appears to depend on the confluency at which the cells are seeded, indicating proximity to one another as a potential mediator. Additionally, mouse mammary epithelial EpH4 Mito-GFP cells were cultured with mouse MMTV-*neu* RFP mammary cancer cells. In all cases, mitochondrial transfer was seen from the normal epithelial cells to the cancer cells within 24 h (Fig. 5A–C). However, fewer events were seen between mouse EpH4 Mito-GFP and MMTV-*neu* cells (Table 1). Adjusting the ratio of MCF-12a to human cancer cell lines from 2:1 to 5:1 MCF-7 and MDA-MB-231 did not affect the amount of transfer (not shown).

### Tunneling nanotubes are the primary means of transfer of mitochondria between normal breast epithelial and breast cancer cells

Mitochondrial transfer can occur through numerous mechanisms depending on cell type, proximity, and cellular environment [16]. After establishing the occurrence and frequency of mitochondrial transfer between various mammary epithelial and cancer cells, we investigated multiple mechanisms to determine how these events occur.

Tunneling nanotubes (TNTs) are a common mechanism for mitochondrial transfer in somatic and stem cells [24–26]. Using fluorescent microscopy, we were able to capture multiple instances in both 2D and 3D cultures where donor epithelial mammary cells form bridge-like structures containing GFP-labeled mitochondria and contact recipient tumor cells consistent with TNT transfer (Fig. 6A–D).

To further establish TNT as a mechanistic method for mitochondrial transfer, we used cytochalasin D, an actin polymerization inhibitor required for TNT formation. After cytochalasin D treatment, the MCF-12a Mito-GFP and MCF-7 RFP cocultures were fixed and stained using Phalloidin-iFluor 555 reagent to visualize actin filament formation (Fig. 6E). Cell cultures containing cytochalasin D showed a strong statistically significant decrease in the recorded number of mitochondrial transfer events (\*\*\*\**P* < 0.0001) (Table 1). This demonstrates that inhibiting TNT formation decreases the transfer of mitochondria between cells. Additionally, in correlation with the observed number of mitochondrial transfers, no bridge-like actin filaments were recorded between cells in cytochalasin D treatments as compared to the control group.

Although actin polymerization was hindered using cytochalasin D, there was still evidence of a minor amount of mitochondrial transfer seen within the 2D cocultures. Due to these results, we explored extracellular transfer (e.g., extracellular vesicles (EVs)) as a potential secondary mechanistic method for mitochondrial transfer. MCF-12a conditioned medium was filtered through a 0.22 µm filter and added to MCF-7 cultures, which showed evidence of mitochondrial transfer in all human and mouse cancer cell types (Fig. 6F–H). Importantly, the number of total EV-related mitochondrial transfer events recorded in this experiment was similar to the mitochondrial transfers that remained following the inhibition of TNTs. Therefore, nondirect cell transfer mechanisms, such as EVs, are only a minor contributor to mitochondrial transfer in this system (Table 1).

To enhance visualization of EVs, we used an RFP-DiI stain to fluorescently mark lipophilic membrane of the donor cells (Fig. 7A). Importantly, once we again exposed cancer cells to filtered, conditioned media, the presence of RFP fragments (approximately 0.2–0.1 µm in diameter) was seen integrated into the recipient cells (Fig. 7B). The number of fluorescent particles integrated into the membranes of recipient cells was directly correlated with the frequency of observed



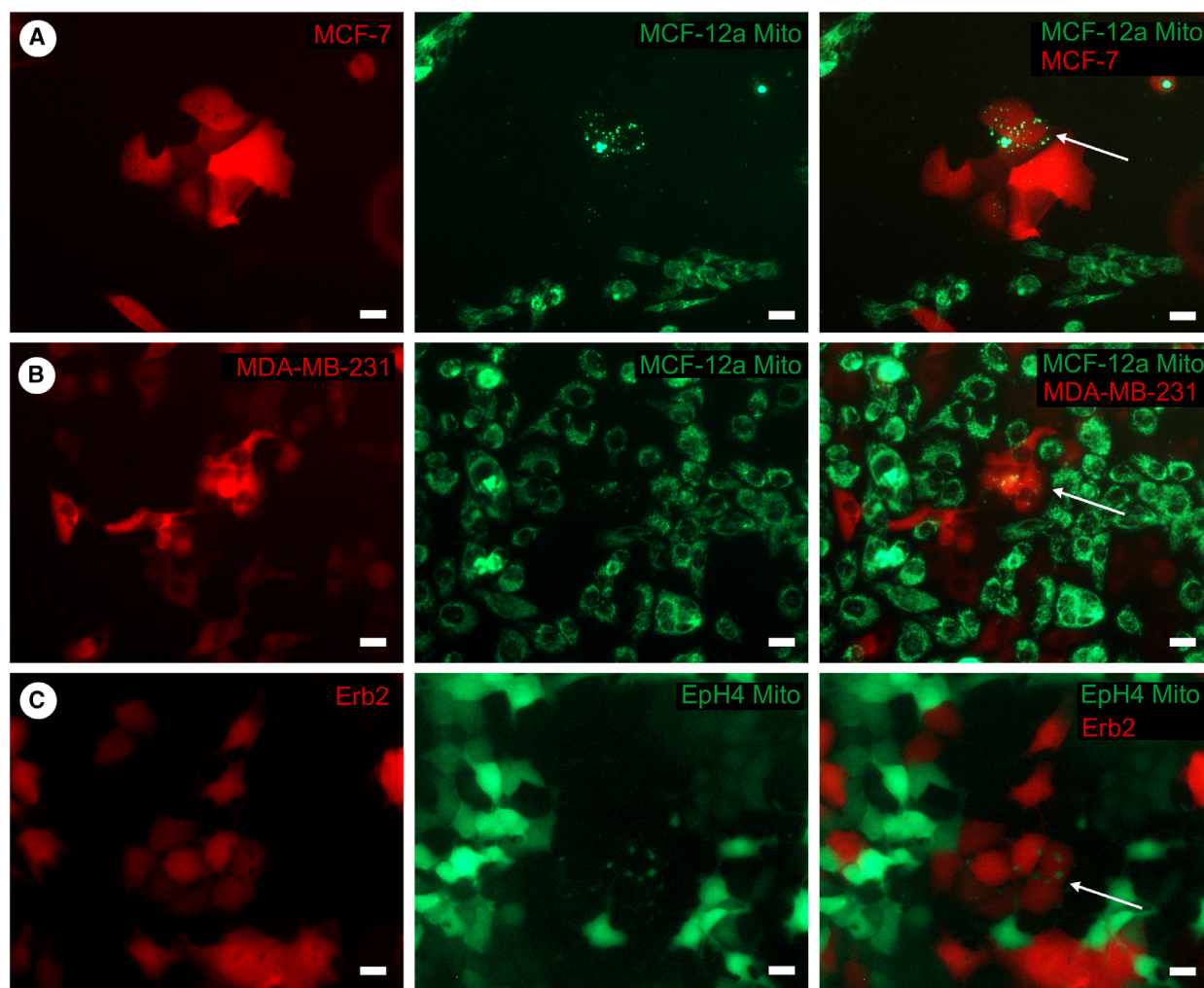
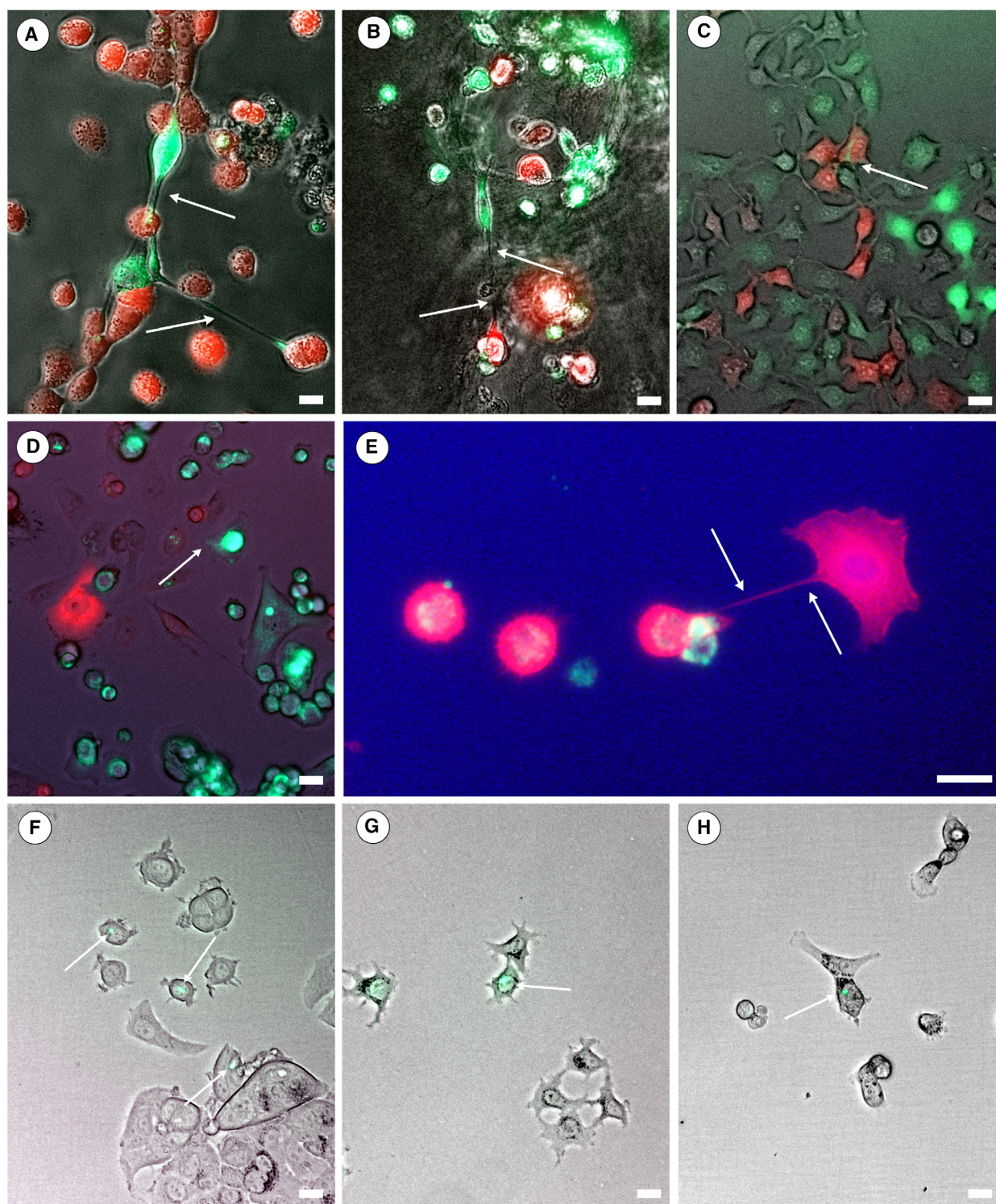


**Fig. 5.** Mitochondrial transfer from epithelial to cancer cells in 2D. (A, B) Human mammary epithelial MCF-12a-Mito-GFP derived mitochondria (green) integrated into MCF-7 RFP (A) and MDA-MB-231 RFP (B) cells when cocultured in a 2:1 ratio. Figure representative of 25 cells (A) and 88 cells (B) obtained from 15 (A) and 3 (B) independent experiments. (C) Mouse mammary epithelial EpH4 Mito-GFP derived mitochondria (green) integrated into mouse MMTV-*neu* RFP cancer cells when cocultured in a 2:1 ratio. Figure representative of 75 cells obtained from 3 independent experiments. White arrows showing GFP-labeled mitochondria (green) integrated into RFP-labeled (red) recipient cell types. Scale bars = 20  $\mu$ m.

**Fig. 6.** Mitochondria are transferred from MCF-12a to cancer cells by tunneling nanotubes and extracellular vesicles (A, B) White arrows showing example of tunneling nanotube formation between MCF-12a Mito-GFP (green) and MCF-7 RFP (red) cells in 2D (A) and 3D (B) microenvironments. Images captured 24 h postinitial coculturing. Figure representative of 38 cells (A) and 29 cells (B) obtained from 15 (A) and 4 (B) independent experiments. (C) White arrows showing example of tunneling nanotube formation between mitochondrial-labeled EpH4 Mito-GFP (green) and MMTV-*neu* RFP (red) cells in 2D coculture. Image captured 48 h post initial coculturing. Figure representative of 72 cells obtained from 3 independent experiments. (D) White arrow showing example of tunneling nanotube formation between MCF-12a Mito-GFP and MDA-MB-231 RFP (red) cells in 2D culture. Image captured 72 h after initial coculturing. Figure representative of 57 cells obtained from 3 independent experiments (E) Image of phalloidin staining of 2D formalin-fixed culture. White arrows showing F-actin (red) tunnel formation between MCF-7 BFP (blue) and MCF-12a-Mito-GFP (green). Figure representative of 6 cells obtained from 2 independent experiments. (F–H) MCF-7 (F), MMTV-*neu* (G), and MDA-MB-231 (H) cells were treated with filtered conditioned medium from MCF-12a Mito-GFP (F, H) and EpH4 Mito-GFP (G) cultured cells. White arrows showing GFP-labeled (green) mitochondria integrated in recipient cells. Figure representative of 48 cells (F) 7 cells (G) 13 cells (H) obtained from 6 (F) 3 (G, H) independent experiments. Scale bar = 20  $\mu$ m.





mitochondria within the cell. To further establish EVs as a mechanism for mitochondrial transfer, we used the ROCK inhibitor Y-27632, which inhibits microvesicle and exosome communication within the cellular environment [27]. Interestingly, a strong statistically

significant decrease in both the recorded number of mitochondrial transfer events ( $***P < 0.001$ ) and the amount of RFP extracellular fragments ( $***P < 0.001$ ) was observed when the DiI-stained donor epithelial breast cells were exposed to ROCK inhibitor Y-27632



**Fig. 7.** Indirect transfer of mitochondria from MCF-12a cells to cancer cells, likely mediated by EVs. (A) 20× fluorescent image. White arrows indicating RFP-labeled extracellular vesicles isolated from MCF-12a Mito-GFP media. (B) 20× fluorescent image. White arrows indicating integrated RFP-labeled EV and GFP mitochondrial transfer in recipient MCF-7 cell. (C) Quantification of the mean quantity of DiI-RFP EVs detected in recipient MCF-7 cells with and without addition of 10  $\mu$ M of ROCK inhibitor ( $***P < 0.001$ ;  $n = 1024$ ). (D) Quantification of the mean quantity of GFP mitochondrial transfer detected in recipient MCF-7 cells with and without addition of 10  $\mu$ M of ROCK inhibitor ( $***P < 0.001$ ;  $n = 1024$ ). Error bars display standard deviation (SD) of the mean. All statistical data were analyzed using an unpaired *t*-test. Scale bar = 20  $\mu$ m.

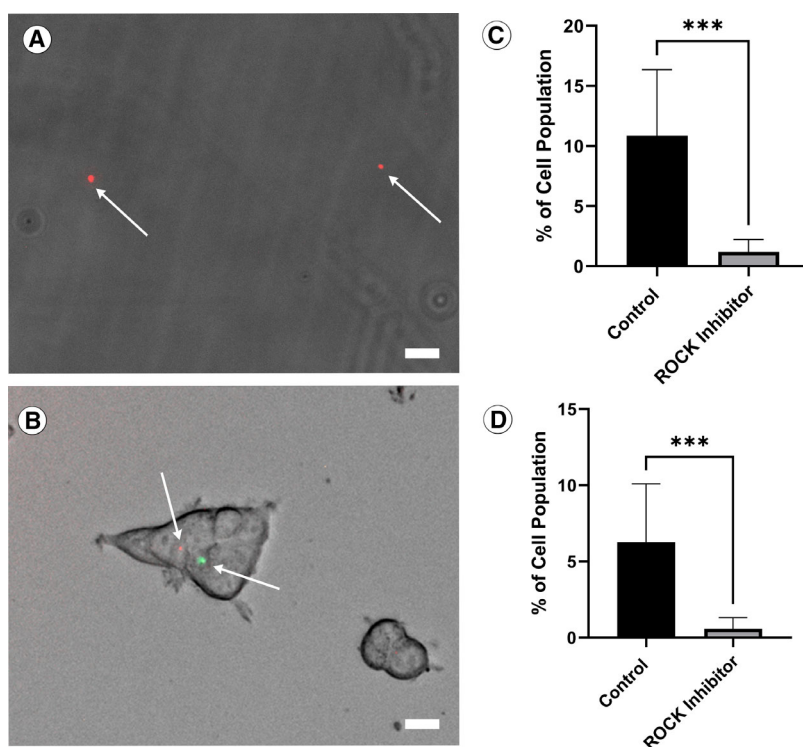


(Fig. 7C,D). The percentage of DiI-incorporated recipient cells decreased from approximately 10.53% in control cell cultures to 0.97% in cultures containing ROCK inhibition (Fig. 7C). Similarly, mitochondrial transfer evidence decreased from 6.26% to 0.58% (Fig. 7D) (Table 1).

### Mitochondrial transfer causes metabolic changes in mammary cancer cells

Next, we investigated the metabolic effects of mitochondrial transfer. First, we evaluated changes in ATP production using a designed live stain (ATPBiotracker Red-1). MCF-7 cells were transduced with a constitutive blue fluorescent protein (BFP) marker so we could subsequently identify both the copGFP-mitochondria and the red ATPBiotracker dye. The results showed a statistically significant decrease in ATP production in cells that had been 2D cocultured with MCF-12a Mito-GFP cells compared to the control MCF-7 BFP cultured cells (Fig. 8A). Likewise, 2D MDA-MB-231 BFP cocultured with MCF-12a Mito-GFP cells displayed significantly lower levels of ATP production when compared to their control group (Fig. 8B). Furthermore, it was found that when MCF-7s showed evidence of mitochondrial transfer, they held an even lower level of ATP production (Fig. 8A). Similar

trends were also seen in 3D chimeric organoids where MCF-7 cells integrated with MCF-12a cells showed a statistically lower amount of ATP production compared to control MCF-7 cells (Fig. 8C).

We used live cell staining for reactive oxygen species (ROS) detection as a secondary metabolic assessment. Interestingly, the results indicated a statistically significant decrease in ROS production in MCF-7 cells that had been cocultured with MCF-12a Mito-GFP cells compared to MCF-7 cultured by themselves (Fig. 8D). Similar results were found when culturing MDA-MB-231 and MCF-12a cells (Fig. 8E). ROS levels in MCF-7 cells with mitochondrial transfer declined but were not statistically significant when compared to the control group (Fig. 8D). The MDA-MB-231 cells containing donor mitochondrial showed a statistically significant decrease when compared to the control group (Fig. 8E). It is important to note that due to the nature of the nuclear label, we cannot rule out that MCF-7 cells lacking detectable GFP mitochondria did not contain donated mitochondria. Overall, these results are consistent with a decrease in metabolic activity following coculture and mitochondrial transfer.

Lastly, we sought to isolate cells displaying mitochondrial transfer to evaluate changes in metabolic-related gene expression. Using FACS, we successfully isolated MCF-7 cells that had taken up Mito-GFP and those



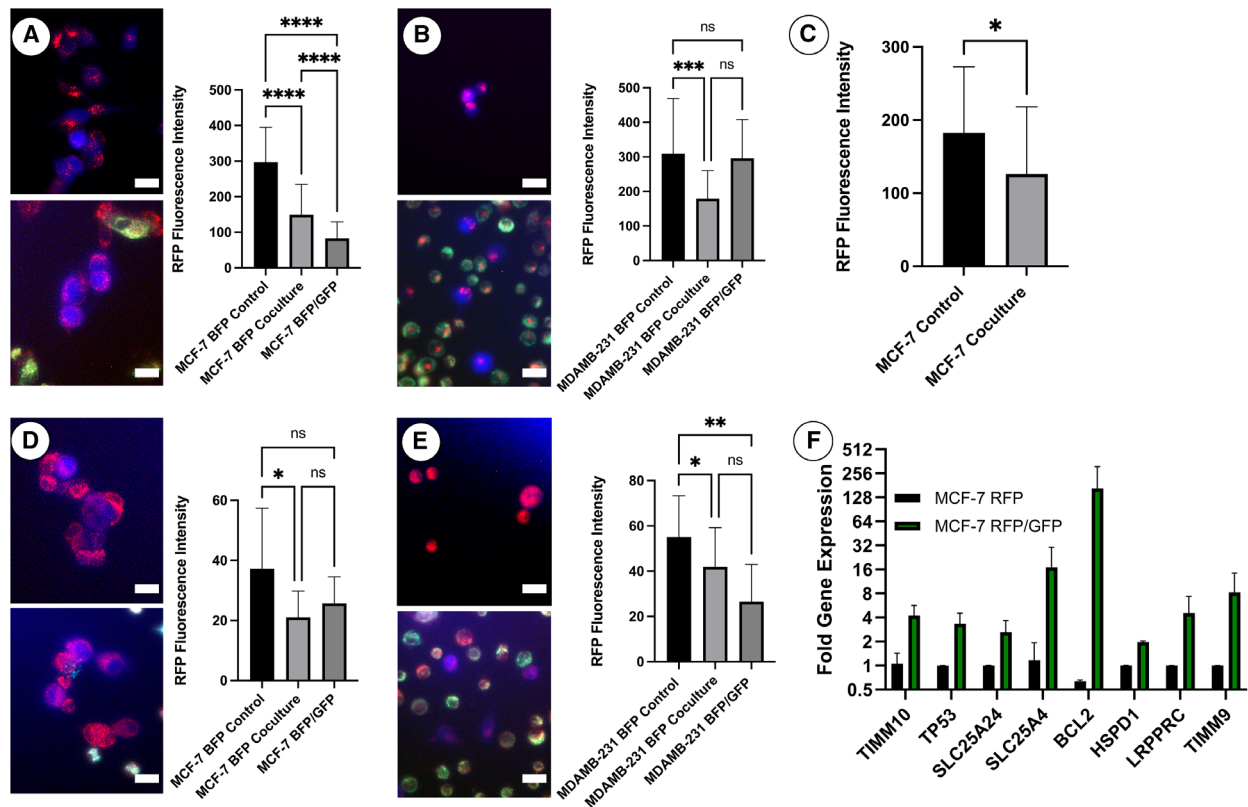


**Fig. 8.** Mitochondrial transfer causes metabolic changes in mammary cancer cells. (A, B) Representative image (left) and fluorescence quantification (right) of 2D MCF-7-BFP (blue) (A) and MDA-MB-231-BFP (blue) (B) from control and MCF-12a Mito-GFP cocultures live stained with ATPBiotracker Red-1 (red). Figure representative of 11 cells (control) 10 cells (coculture) (A) and 3 cells (control) 39 cells (coculture) (B) obtained from 3 independent experiments. (C) Quantification of the mean fluorescent intensity of ATP production in 3D bioprinted cultures comparing MCF-7 control and MCF-12a/MCF-7 coculture populations. (D, E) Representative image (left) and fluorescence quantification (right) of 2D MCF-7 (blue) (D) and MDA-MB-231 (blue) (E) from control and MCF-12a Mito-GFP (green) cocultures live stained with CellRox™ (red). Figure representative of 15 cells (control) 8 cells (coculture) (D) and 5 cells (control) 27 cells (coculture) (E) from 3 independent experiments. (F) Gene expression analysis of significantly altered mitochondrial genes between FACS-isolated populations of MCF-7 cells with Mito-GFP from MCF-12a donors and MCF-7 cells that lacked Mito-GFP. Figure obtained from 3 independent experiments of both MCF-7 RFP and MCF-7 RFP/GFP. Error bars display standard deviation (SD) of the mean. Statistical data were analyzed using one-way analysis of variance (ANOVA) with Tukey's multiple comparisons test. Additionally, an unpaired *t*-test was used for 3D data analysis. Scale bars = 20  $\mu$ m. \**P* < 0.05; \*\**P* < 0.01; \*\*\**P* < 0.001; \*\*\*\**P* < 0.0001; ns, nonsignificant.

that did not in 2D cocultures with MCF-12a cells. We performed qRT-PCR targeting mitochondria-associated genes. It was determined that MCF-7 cells containing donor mitochondria displayed significant gene upregulation in several genes associated with metabolic activity (Fig. 8F). Upregulation was observed in multiple genes including TIMM9, TIMM10, SLC25A24, SLC25A4, HSPD1, LRPPRC, BCL2, and TP53. Importantly, all these genes are nuclear-encoded, demonstrating the transfer was impacting nuclear gene control.

## Discussion

The normal mammary microenvironment contains signals sufficient to redirect cancer and stem cells to a

normal mammary epithelial progenitor cell fate. This aspect of the normal microenvironment is understudied and of paramount importance, as preventative/suppressive therapies could shield women from the trauma of breast cancer. Here, we have uncovered some of the first molecular mechanisms driving the redirection process.

Our specialized low-cost 3D bioprinter is currently the only effective way to translate chimeric organoids into an *in vitro* environment due to the difficulties in generating repeatable chimeric organoids in standard 3D culture. With our system, we can alter the specifics of tumoroid and chimeric organoid formation down to micron variations and single-cell resolutions. This study uses this system to demonstrate that signals from

normal epithelium can have an immediate but sustained effect on breast cancer cell proliferation. These data show that through cell-to-cell transfer, metabolic alterations result from the uptake of epithelial donor mitochondria, causing breast cancer cells to return to a more 'epithelial-like' state by stabilizing mitochondrial function and prohibiting excessive proliferation. However, it should be noted that we are not claiming mitochondrial transfer alone can account for all the observed effects of cancer cell redirection. This is why cancer cells derived from chimeras both *in vivo* [7] and *in vitro* (Fig. 1) produce tumors/tumoroids when removed from the normal mammary microenvironment but grow at a significantly reduced rate. Interestingly, extracellular matrix extracts from the mammary gland are sufficient to differentiate nonmammary stem cell populations within the context of the mammary fat pad *in vivo* to produce functional mammary glands [9], but the redirection of cancer cells requires the presence of functional mammary epithelium [6,7]. Based on our findings, mitochondrial transfer helps alter metabolism to reduce growth and decrease proliferative markers, such as Ki67, allowing for microenvironmental redirection. Additionally, apoptosis was decreased in coculture MCF-7 cells. The mammary epithelial microenvironment appears to be inhibiting proliferation resulting in decreased tumor formation. However, cells do not appear to be more susceptible to apoptosis. This is consistent with *in vivo* findings showing that although human cancer cells undergo reprogramming within mouse mammary microenvironments, they do not appear apoptotic and, therefore, remain a normalized cell type that contributes to mouse mammary gland formation [6,7].

Importantly, additional signals from normal epithelium, such as miRNA, signaling molecules, can also be transferred between cells in TNTs or EVs are likely important and something we are continuing to study. However, our studies' effect on tumoroid growth is evidence of sustained metabolic effects. Therefore, we interpret these results to mean that mitochondrial transfer is likely a key component of microenvironmental redirection, allowing for metabolic 'stabilization' of the cancer cells and sensitizing them to normal growth/death signals within the mammary gland. Future studies will explore this in more detail by evaluating the additional effects of ECM and extracellular signaling on the process.

A limitation in the current study is that due to the labeling system employed, not all events of mitochondrial transfer between the donor and recipient cells can be successfully identified, nor is the extent of mtDNA transfer evident. Because the Mito-GFP label is

nuclear-encoded, the GFP signal will diminish after the transfer, so the current study cannot determine if the donor mitochondria and mtDNA expand within the recipient cell. We aim to further research these questions as understanding the genetic exchange and cell signaling of mitochondrial transfer is critical to further understanding its role in microenvironment cellular communication and downstream disease effects.

Mechanistically, we demonstrated here that mitochondrial transfer in our system occurs primarily through TNTs, although minor additional contribution comes from extracellular transfer. Notably, the difference between the percentage of mitochondrial transfer observed when TNT was inhibited with the percentage of observed extracellular events correlates to total transfer events. Thus, based on the recorded events and calculated frequencies found in Table 1, it can be concluded that while extracellular transfers play a role in mitochondrial transfers, TNT is the primary mechanism. This extracellular transfer is consistent with EVs as we demonstrate the transfer of membrane-containing structures that can be inhibited by ROCK inhibitor, which blocks microvesicle formation. Future studies will seek to more carefully define extracellular cargo and EV characteristics to better understand the mechanisms of mitochondrial transfer within this system.

Finally, the metabolic organelle exchange significantly affects nuclear-encoded mitochondrial genes in cancer cells that have undergone mitochondrial transfer. Specifically, we observed upregulation in p53, an important tumor suppressor that regulates genes involved in cell cycle arrest, cell death (apoptosis), DNA repair, and senescence [28]. Additionally, a significant upregulation was found in B-cell lymphoma 2 (Bcl-2). These are a family of proteins that are key regulators with pro- and anti-apoptotic activities and are held in a fine, delicate balance in healthy cells [29]. Depending on the precise composition of BCL-2 family members in a cell, the acute release of pro-apoptotic proteins could activate the apoptotic cascade, making the cells more susceptible to cell death and limiting cell proliferation. We hope to conduct further studies to explore the changes and effects of metabolic gene expression regarding mitochondrial transfer in cancer cells.

To the best of our knowledge, this is the first description of a 3D bioprinter-assisted system for studying mitochondrial transfer within organoids. Furthermore, this study is the first to demonstrate major mechanistic insights into the process of mammary microenvironmental redirection of breast cancer and the first step toward the potential translational benefit of this remarkable phenomenon.

## Materials and methods

### Cell culture

MCF-7 breast cancer cells (RRID: CVCL\_0031) are both estrogen receptor and progesterone receptor positive while also belonging to the luminal A molecular subtype [30]. MDA-MB-231 cells (CVCL\_0062) were also used as a comparative triple-negative human breast cancer cell line. MMTV-*neu* cells are mouse mammary cancer cells. For MECs, a nontumorigenic human MCF-12A (RRID: CVCL\_3744) and mouse EpH4-EV (RRID: CVCL\_S648) epithelial breast cell lines were used. All cell lines were purchased from the American Type Culture Collection (ATCC), with the exception of the MMTV-*neu* cell line that was generously gifted by Dr. Brian Booth at Clemson University [31]. MCF-7, MDA-MB-231, MMTV-*neu*, and EpH4 cells were cultured in Dulbecco's modified Eagle's medium (DMEM) containing GlutaMAX supplement (Gibco, Gaithersburg, MD, USA). The DMEM was supplemented with 10% fetal bovine serum (Gibco) and 1% antibiotic-antimycotic (100×) (ABAM; Life Technologies, Carlsbad, CA, USA). MCF-12a cells were cultured in DMEM/F12 with GlutaMAX (Gibco), supplemented with 5% horse serum (Gibco), 10  $\mu\text{g}\cdot\text{mL}^{-1}$  bovine insulin (Millipore Sigma, St. Louis, MO, USA), 500  $\text{ng}\cdot\text{mL}^{-1}$  hydrocortisone (Millipore Sigma), 1% ABAM, and 20  $\text{ng}\cdot\text{mL}^{-1}$  human epidermal growth factor (hEGF; Gibco). All cells were cultured in an incubator at 37 °C with 5%  $\text{CO}_2$ . All experiments were performed with mycoplasma-free cells.

### Mito-GFP lentivirus system

MCF-7 and MMTV-*neu* cells were transduced with CAG RFP expressing lentivirus (Cellomics Technology, Halethorpe, MD, USA). MCF-12a and EpH4 cells were transduced using Mitochondria Cyto-Tracer™ pCT-Mito-GFP (CMV) (System Biosciences, Palo Alto, CA, USA). A multiplicity of infection (MOI) of 10 was determined for successful transduction. The lentivirus remained in the media for 72 h whereafter the cells were passaged at a 1 : 4 split. After 24 h, 1000  $\text{ng}\cdot\text{mL}^{-1}$  of puromycin (Millipore Sigma) was added to the media to select successfully transduced cells. The cells were observed for fluorescence using a Zeiss Axion Observer microscope. Several images were captured randomly across 2D plates. All RFP-labeled recipient cells were counted. Furthermore, all RFP-labeled cells containing evidence of GFP mitochondrial fragments were quantified to determine an average percentage of mitochondrial transfer found within 2D cell cultures of breast epithelial and cancer cells.

### 3D bioprinting system

All chimeric organoids and tumoroids were made using our novel 3D bioprinting system [12,15,23]. Cells were diluted

in culture medium to a concentration of 10 million cells·mL<sup>-1</sup> and 3D printed into a 24-well plate containing 700  $\mu\text{L}$  of 1.5 mg·mL<sup>-1</sup> three-dimensional hydrogels made from high concentration rat tail collagen (Corning Life Sciences, Durham, NC, USA) per well. Using a P-1000 micropipette puller (Sutter Instruments, Novato, CA, USA), 25–50  $\mu\text{L}$  glass needles (Drummond Scientific, Broomall, PA, USA) were pulled to a tip of 100  $\mu\text{m}$  as previously described [15]. Roughly 100 cells were placed into each injection site with a ratio of 2 : 1 normal to tumorigenic cells in a 3 × 10 grid, 300  $\mu\text{m}$  distance between each column and 1.5 mm between each row. The number of cells and ratio of cancer to normal cells was based on previous optimization [12,14,23]. After printing, 500  $\mu\text{L}$  MCF-12a cell culture medium was added to each well. The samples were incubated at 37 °C, and the medium was changed every 2–3 days.

### Immunohistochemistry/immunofluorescence

For immunofluorescence assays of 2D cultures, cells were cultured in a 24-well tissue culture plate for 48 h. The media was aspirated, and the cells were rinsed in PBS. The cells were fixed in 10% formalin added for 15 min. The cells were then rinsed thrice with PBS at 5 min each. For permeabilization, 500  $\mu\text{L}$  of ice-cold methanol was added for 10 min at −20 °C. The samples were then rinsed with PBS thrice as similarly described. 10% goat serum was used to block samples for 1 h. The goat serum was then aspirated, and the primary antibody was added to the sample(s) at 4 °C overnight. The samples were rinsed with TBS/0.1% tween (Sigma Millipore) thrice followed by one wash of 1× TBS for 5 min. For 3D cell culture, samples were fixed in 10% formalin for one hour and embedded in paraffin and sectioned. Sections were deparaffinized with xylenes then rehydrated. Slides were rinsed in 1× TBS and transferred to preheated antigen retrieval buffer for 20 min. The samples were cooled and rinsed twice in 1× TBS. After cooling, the samples were treated similarly to the immunofluorescence samples, starting with 10% goat serum for blocking. The following primary antibodies were used: RFP Monoclonal Antibody (RF5R) (Invitrogen, cat # MA5-15257, dilution 1:500, Waltham, MA, USA), Turbo GFP Polyclonal Antibody (Invitrogen, cat # PA5-22688, dilution 1:100, Waltham, MA, USA), and anti-Ki67 (Abcam, Cambridge, UK, cat # ab15580, dilution 1:100). Primary antibodies were diluted in 0.5% goat serum and incubated overnight in humidified chambers at 4 °C. Negative controls with 0.5% goat serum alone. Secondary antibodies were as follows: Alexa Fluor™ 488 goat anti-rabbit IgG (H + L) (Invitrogen, cat # A11034, dilution 1:1000, Waltham, MA, USA), Alexa Fluor™ 568 goat anti-mouse IgG (H + L) (Invitrogen, cat # A11031, dilution 1:1000, Waltham, MA, USA), and Alexa Fluor™ 350 goat anti-rabbit IgG (H + L) (Invitrogen, cat # A11046, dilution



1:500, Waltham, MA, USA). Secondary antibodies were diluted in 0.5% goat serum, placed on the samples, and incubated at room temperature in a dark, moist environment for 1 h. Slides were counterstained with DAPI. Images were obtained using a Zeiss Axion Observer microscope at 10 $\times$  and 20 $\times$  magnification. The frequency of mitochondrial transfer from 3D cultures was determined similarly to that of live 2D cultures. For immunofluorescence staining for Ki67, images were captured and Ki67 fluorescent intensity of the cells was measured using a Zeiss Axion Observer microscope and Zeiss Zen software.

### Gene expression analysis

BD Biosystems Influx<sup>TM</sup> FACS was used to separate cocultured cell populations based on RFP or Mito-GFP expression. After completion of cell sorting, RNA extraction was performed on desired isolated cell populations using RNeasy spin columns (Qiagen, Germantown, MD, USA) according to the manufacturer's protocol. Following RNA extraction, cDNA was reverse transcribed using a High-Capacity Reverse Transcription cDNA Kit (Thermo Fisher Scientific) and Arktik thermocycler (Thermo Fisher Scientific). Using a StepOne Plus Real-Time PCR System (Applied Biosystems, Waltham, MA, USA), mitochondrial TaqMan fast custom arrays (Thermo Fisher Scientific) were used to perform gene expression analysis. All samples were compared against MCF-7 RFP relative control samples. Endogenous genes included  $\beta$ -actin, GAPDH, and S18. All fold gene expressions were calculated using  $\Delta\Delta$ CT methodology.

### Live metabolic staining

2D cell cultures were plated in 6-well plates at 80% confluency and incubated for 36 h until 90%–100% confluency was reached. CellRox<sup>TM</sup> Orange (Thermo Fisher Scientific) was combined with media for a final concentration of 5  $\mu$ M. Each well received 2 mL of the media/CellRox cocktail and was incubated at 37  $^{\circ}$ C for 30 min. Alternatively, ATPBiotracker Red-1 (Sigma Millipore) was combined with media for a final concentration of 10  $\mu$ M. Each well received 2 mL of the media/ATPBiotracker cocktail and was incubated at 37  $^{\circ}$ C for 15 min. The cells were then rinsed thrice with DPBS. Images were captured and DsRed Fluorescent intensity of the cells was measured using a Zeiss Axion Observer microscope and Zeiss Zen software.

Using a 24-well plate, unlabeled MCF-12a and MCF-7 RFP cells were bioprinted into rat tail collagen hydrogels at a 2 : 1 ratio, respectively. The cell cultures were incubated and observed for organoid formation for approximately 10–14 days. ATPBiotracker Red-1 was combined with cellular media for a final concentration of 20  $\mu$ M. The prints were then incubated for 20 h at 37  $^{\circ}$ C. The live stain was removed, and the gels were incubated with their

respective medium for an additional 7 h. Following this, the hydrogels were incubated with collagenase IV (Gibco) for 20–30 min for ECM digestion. The cells were then centrifuged and rinsed with DPBS thrice whereafter they were placed on a slide. Images were captured and DsRed Fluorescent intensity of the cells was measured using a Zeiss Axion Observer microscope and Zeiss Zen software.

### Tunneling nanotubes

Tunneling nanotube experimentation was conducted using cytochalasin D (Santa Cruz Biotechnology, Dallas, TX, USA) for actin polymerization prevention. The cytochalasin D was dissolved at 25 mg·mL<sup>-1</sup> in DMSO whereafter multiple cytochalasin concentrations varying from 50 nM to 200 nM were used to assess cell toxicity. MCF-7 BFP and MCF-12a Mito-GFP were cocultured in MCF-12a media containing either 50 nM or 100 nM of cytochalasin D in a 1 : 2 cell ratio, respectively. The cells were seeded at 80% confluency on 6-well tissue culture plates. After 24 h, the samples were fixed in 10% formalin for 15 min, rinsed in PBS, and stained for actin filaments using Phalloidin-iFlour 555 reagent (Abcam). A 1000 $\times$  working solution was made according to the manufacturer's protocol. The samples were imaged using a Zeiss Axion Observer microscope at 10 $\times$ . Tunneling nanotube events were recorded in each sample.

### Extracellular vesicles

To evaluate the presence of extracellular vesicles and its effect on the frequency of mitochondrial transfer, MCF-7, MMTV-*neu*, MDA-MB-231, Eph4 Mito-GFP, and MCF-12a Mito-GFP cells were cultured separately. After 24 h, the media from the MCF-12a culture was collected and filtered using a 0.2  $\mu$ M SFCA cell strainer (Corning). The media was then used on the MCF-7 and the MDA-MB-231 recipient cells. Similarly, Eph4 media was collected and filtered onto MMTV-*neu* cultures. After an additional 24 h, the recipient cells were imaged for the presence of GFP-labeled mitochondrial fragments. The media switch occurred every 24 h over a 3-day period.

Additionally, for fluorescent labeling for EV detection, MCF-12a Mito-GFP cells were labeled with the lipophilic membrane stain DiI (1,10-dioctadecyl-3,3',3'-tetramethylindocarbocyanine perchlorate;  $\lambda_{Ex}/\lambda_{Em}$  = 549/565 nm) (Invitrogen, Thermo Fisher Scientific, Waltham, MA, USA) according to the manufacturer's protocol. Briefly, cells were trypsinized using TrypLE and cultured in DMEM/F12 with GlutaMAX at a concentration of  $1 \times 10^6$  cells·mL<sup>-1</sup>. 5  $\mu$ L of the dye solution (1 mM) was added to 1 mL of cell suspension. The cells were incubated for 20 min at 37  $^{\circ}$ C in the dark and then centrifuged at 300 *g* for 5 min at room temperature. The stained cell pellet obtained was further subjected to two rounds of centrifugation in PBS to remove

unbound dye. Cells were plated at confluency in a 12-well plate (Santa Cruz Biotechnology) in MCF-12a growth media. For extracellular vesicle inhibition, 10  $\mu\text{M}$  of Y-27632 (StemCell Technologies, Vancouver, Canada) was added to the media. The cells were maintained in culture for 18 h before starting EV collection. MCF-12a media was filtered and collected as previously described. The recipient cells were imaged and quantified for the presence of GFP-labeled mitochondrial protein and DiI-RFP-stained membrane as previously described.

### Apoptosis detection

Unlabeled MCF-12a and MCF-7 RFP cells were cultured in a 24-well plate using 12a media as similarly described. Unlabeled MCF-7 and MCF-7 RFP cells were cultured as a control. The cells were plated at confluency. After 48 h, the cells were treated with 1500  $\text{ng}\cdot\text{mL}^{-1}$  of puromycin for MCF-7 RFP selection. After an additional 48 h of puromycin treatment, dead cells and debris were discarded. The remaining cells were rinsed thrice in PBS. Annexin-binding buffer (Thermo Fisher Scientific) was diluted from 50 $\times$  to 10 $\times$  using sterile water. The sample cells were then detached using tryPLE and resuspended in annexin-binding buffer. The cell density was adjusted to  $1 \times 10^6$  cells $\cdot\text{mL}^{-1}$  whereafter 100  $\mu\text{L}$  of cell suspension was transferred into new Eppendorf tubes. 15  $\mu\text{L}$  of Annexin V conjugate Alexa Fluor<sup>TM</sup> 488 (Thermo Fisher Scientific) was then added to each tube and incubated for 15 min at room temperature. The cells were washed with annexin-binding buffer and mounted onto a slide for fluorescence detection. Using a Zeiss Axion Observer microscope at 10 $\times$ , the cells were imaged, and the number of GFP fluorescent cells were counted evaluated and compared between the control and cocultured samples.

### Tumor growth rate analysis

MCF-7 RFP and MCF-12a cells were 3D bioprinted into rat tail collagen hydrogels in a 1 : 2 ratio, respectively, 50 cells per injection. MCF-7 RFP and unlabeled MCF-7 cells were bioprinted with the same parameters as a control group. The cells were incubated at 37  $^{\circ}\text{C}$ , 5%  $\text{CO}_2$  for 7 days with MCF-12a media, changed every 2–3 days, to allow for organoid/tumoroid formation. After day 7, each printed well was treated with DMEM/FBS or MCF-12a media containing 1000–4000  $\text{ng}\cdot\text{mL}^{-1}$  of puromycin. The tumoroid structures were assessed and measured based on their volume and DsRed fluorescence intensity over 7 days using Zeiss Axion Observer microscope at 10 $\times$  and Zeiss Zen software.

Similarly, MCF-7 RFP and MCF-12a cells were cultured in a T25 flask at a 1:2 ratio for 5 days in MCF-12a media. When the cells reached 80% confluency, 1500  $\text{ng}\cdot\text{mL}^{-1}$  of puromycin was added to the media of the 2D cell culture. The cells were exposed to the puromycin treatment for

2 days, and the media was changed after 24 h. Dead cells and debris were discarded. The remaining cells were trypsinized and washed thrice with 1 $\times$  DPBS, whereafter they were printed into rat tail collagen hydrogels with approximately 50 cells per injection. The cells were incubated at 37  $^{\circ}\text{C}$ , 5%  $\text{CO}_2$  for 7 days with MCF-12a media containing 1500  $\text{ng}\cdot\text{mL}^{-1}$  puromycin to allow for organoid formation. The development of tumoroid structures were measured as previously described.

MCF-7 RFP and MCF-12a Mito-GFP cells were cocultured in a 1 : 2 ratio, respectively. The cells were cultured as previously described in T75 flasks. Additionally, MCF-7 cells were cultured using MCF-12a media as a positive control. The cells were seeded at 70–80% confluency. After 48 h, the cells were trypsinized and sorted using a BD Biosystems Influx<sup>TM</sup> FACS. RFP+ cell populations were collected and immediately printed into rat tail collagen hydrogels as previously described using the 3D bioprinter. The development of tumoroid structures were assessed and measured based on their areas over a 17-day period using Zeiss Axion Observer microscope at 10 $\times$  and Zeiss Zen software.

### Statistical analysis

Statistical analysis and graphical representation were performed using Prism 10 software. Single statistical comparisons were performed using Student's *t*-test, and multiple comparisons were evaluated by chi-squared statistical hypothesis testing and repeated measures one- and two-way analysis of variance (ANOVA) with a Tukey or Dunnett's post hoc when applicable. All graphical representations display average measured means along with error bars representing the standard deviation of the data.

### Acknowledgements

We would like to thank Yu Jing at the ODU Frank Reidy Research Center for Bioelectrics Core Laboratory for assistance with FACS operations and analysis. We would also like to thank Brian Booth at Clemson University for the donation of the MMTV-*neu* cell line.

### Conflict of interest

The authors declare that the research was conducted in the absence of any commercial or financial relationships that could be construed as a potential conflict of interest.

### Author contributions

JB: conceptualization, data curation, formal analysis, investigation, methodology, writing—original draft,

writing–review and editing. YK: investigation and editing. EP: investigation and editing. PS: conceptualization, data curation, formal analysis, funding acquisition, investigation, methodology, project administration, resources, supervision, validation, visualization, writing–original draft, writing–review and editing. RB: conceptualization, data curation, formal analysis, funding acquisition, investigation, methodology, project administration, resources, supervision, validation, visualization, writing–original draft, writing–review and editing.

## Peer review

The peer review history for this article is available at <https://www.webofscience.com/api/gateway/wos/peer-review/10.1111/febs.70002>.

## Data availability statement

The data that support the findings of this study are available from the corresponding authors [[rbruno@odu.edu](mailto:rbruno@odu.edu); [psachs@odu.edu](mailto:psachs@odu.edu)] upon reasonable request.

## References

- Sachs PC, Mollica PA & Bruno RD (2017) Tissue specific microenvironments: a key tool for tissue engineering and regenerative medicine. *J Biol Eng* **11**, 34.
- Quail DF & Joyce JA (2013) Microenvironmental regulation of tumor progression and metastasis. *Nat Med* **19**, 1423–1437.
- Weigelt B & Bissell MJ (2008) Unraveling the microenvironmental influences on the normal mammary gland and breast cancer. *Semin Cancer Biol* **18**, 311–321.
- Frank-Kamenetskii A, Mook J, Reeves M, Boulanger CA, Meyer TJ, Ragle L, Jordan HC, Smith GH & Booth BW (2023) Correction: induction of phenotypic changes in HER2-positive breast cancer cells in vivo and in vitro. *Oncotarget* **14**, 842.
- Bruno RD & Smith GH (2012) Reprogramming non-mammary and cancer cells in the developing mouse mammary gland. *Semin Cell Dev Biol* **23**, 591–598.
- Bussard KM, Boulanger CA, Booth BW, Bruno RD & Smith GH (2010) Reprogramming human cancer cells in the mouse mammary gland. *Cancer Res* **70**, 6336–6343.
- Bussard KM & Smith GH (2012) Human breast cancer cells are redirected to mammary epithelial cells upon interaction with the regenerating mammary gland microenvironment in-vivo. *PLoS One* **7**, e49221.
- Bruno RD & Smith GH (2011) Functional characterization of stem cell activity in the mouse mammary gland. *Stem Cell Rev Rep* **7**, 238–247.
- Bruno RD, Fleming JM, George AL, Boulanger CA, Schedin P & Smith GH (2017) Mammary extracellular matrix directs differentiation of testicular and embryonic stem cells to form functional mammary glands in vivo. *Sci Rep* **7**, 40196.
- Booth BW, Boulanger CA, Anderson LH & Smith GH (2011) The normal mammary microenvironment suppresses the tumorigenic phenotype of mouse mammary tumor virus-neu-transformed mammary tumor cells. *Oncogene* **30**, 679–689.
- Weigelt B, Ghajar CM & Bissell MJ (2014) The need for complex 3D culture models to unravel novel pathways and identify accurate biomarkers in breast cancer. *Adv Drug Deliv Rev* **69**, 42–51.
- Reid JA, Palmer X-L, Mollica PA, Northam N, Sachs PC & Bruno RD (2019) A 3D bioprinter platform for mechanistic analysis of tumoroids and chimeric mammary organoids. *Sci Rep* **9**, 7466.
- Kim J, Koo B-K & Knoblich JA (2020) Human organoids: model systems for human biology and medicine. *Nat Rev Mol Cell Biol* **21**, 571–584.
- Reid JA, Mollica PA, Bruno RD & Sachs PC (2018) Consistent and reproducible cultures of large-scale 3D mammary epithelial structures using an accessible bioprinting platform. *Breast Cancer Res* **20**, 122.
- Reid JA, Mollica PA, Johnson GD, Ogle RC, Bruno RD & Sachs PC (2016) Accessible bioprinting: adaptation of a low-cost 3D-printer for precise cell placement and stem cell differentiation. *Biofabrication* **8**, 025017.
- Clemente-Suárez VJ, Martín-Rodríguez A, Yáñez-Sepúlveda R & Tornero-Aguilera JF (2023) Mitochondrial transfer as a novel therapeutic approach in disease diagnosis and treatment. *Int J Mol Sci* **24**, 8848.
- Liu D, Gao Y, Liu J, Huang Y, Yin J, Feng Y, Shi L, Meloni BP, Zhang C, Zheng M *et al.* (2021) Intercellular mitochondrial transfer as a means of tissue revitalization. *Signal Transduct Target Ther* **6**, 65.
- Tang LX, Wei B, Jiang LY, Ying YY, Li K, Chen TX, Huang RF, Shi MJ & Xu H (2022) Intercellular mitochondrial transfer as a means of revitalizing injured glomerular endothelial cells. *World J Stem Cells* **14**, 729–743.
- Brestoff JR, Giwa R, Jia W & Field RL (2023) Intercellular mitochondria transfer rescues aerobic respiration in metabolically compromised macrophages in vitro and in vivo. *J Immunol* **210**, 71.01.
- Dong W, Zhang W, Yuan L, Xie Y, Li Y, Li K & Zhu W (2023) Rescuers from the other shore: intercellular mitochondrial transfer and its implications in central nervous system injury and diseases. *Cell Mol Neurobiol* **43**, 1–16.
- Rustom A, Saffrich R, Markovic I, Walther P & Gerdes HH (2004) Nanotubular highways for intercellular organelle transport. *Science* **303**, 1007–1010.



- 22 Spees JL, Olson SD, Whitney MJ & Prockop DJ (2006) Mitochondrial transfer between cells can rescue aerobic respiration. *Proc Natl Acad Sci USA* **103**, 1283–1288.
- 23 Mollica PA, Booth-Creech EN, Reid JA, Zamponi M, Sullivan SM, Palmer XL, Sachs PC & Bruno RD (2019) 3D bioprinted mammary organoids and tumoroids in human mammary derived ECM hydrogels. *Acta Biomater* **95**, 201–213.
- 24 Wang X & Gerdes HH (2015) Transfer of mitochondria via tunneling nanotubes rescues apoptotic PC12 cells. *Cell Death Differ* **22**, 1181–1191.
- 25 Yang F, Zhang Y, Liu S, Xiao J, He Y, Shao Z, Zhang Y, Cai X & Xiong L (2022) Tunneling nanotube-mediated mitochondrial transfer rescues nucleus Pulposus cells from mitochondrial dysfunction and apoptosis. *Oxid Med Cell Longev* **2022**, 3613319.
- 26 Jackson MV, Morrison TJ, Doherty DF, McAuley DF, Matthay MA, Kissenpfennig A *et al.* (2016) Mitochondrial transfer via tunneling nanotubes is an important mechanism by which mesenchymal stem cells enhance macrophage phagocytosis in the in vitro and in vivo models of ARDS. *Stem Cells* **34**, 2210–2223.
- 27 Kim JH, Lee CH & Baek MC (2022) Dissecting exosome inhibitors: therapeutic insights into small-molecule chemicals against cancer. *Exp Mol Med* **54**, 1833–1843.
- 28 Moulder DE, Hatoum D, Tay E, Lin Y & McGowan EM (2018) The roles of p53 in mitochondrial dynamics and cancer metabolism: the pendulum between survival and death in breast cancer? *Cancers* **10**, 189.
- 29 Qian S, Wei Z, Yang W, Huang J, Yang Y & Wang J (2022) The role of BCL-2 family proteins in regulating apoptosis and cancer therapy. *Front Oncol* **12**, 985363.
- 30 Comşa Ş, Cimpean AM & Raica M (2015) The story of MCF-7 breast cancer cell line: 40 years of experience in research. *Anticancer Res* **35**, 3147–3154.
- 31 Park JP, Blanding WM, Feltracco JA & Booth BW (2015) Validation of an in vitro model of erbB2+ cancer cell redirection. *In Vitro Cellular Dev Biol* **51**, 776–786.

## Supporting information

Additional supporting information may be found online in the Supporting Information section at the end of the article.

**Video S1.** Video of 3D bioprinting system.